creative commons
COMMONS DEED

저작자표시-비영리-변경금지 2.0 대한민국

이용자는 아래의 조건을 따르는 경우에 한하여 자유롭게

- 이 저작물을 복제, 배포, 전송, 전시, 공연 및 방송할 수 있습니다.

다음과 같은 조건을 따라야 합니다:

저작자표시. 귀하는 원저작자를 표시하여야 합니다.

비영리. 귀하는 이 저작물을 영리 목적으로 이용할 수 없습니다.

변경금지. 귀하는 이 저작물을 개작, 변형 또는 가공할 수 없습니다.

- 귀하는, 이 저작물의 재이용이나 배포의 경우, 이 저작물에 적용된 이용허락조건을 명확하게 나타내어야 합니다.
- 저작권자로부터 별도의 허가를 받으면 이러한 조건들은 적용되지 않습니다.

저작권법에 따른 이용자의 권리는 위의 내용에 의하여 영향을 받지 않습니다.

이것은 이용허락규약(Legal Code)을 이해하기 쉽게 요약한 것입니다.

Disclaimer

dCollection

ULSAN NATIONAL INSTITUTE OF
SCIENCE AND TECHNOLOGY

Master's Thesis

DESIGN AND ANALYSIS OF HIGH-Q METASURFACES USING MULTIPOLE EXPANSION

Nguyen Thi Hai Yen

Department of Electrical Engineering

Graduate School of UNIST

2020

ULSAN NATIONAL INSTITUTE OF
SCIENCE AND TECHNOLOGY

DESIGN AND ANALYSIS OF HIGH-Q METASURFACES USING MULTIPOLE EXPANSION

Nguyen Thi Hai Yen

Department of Electrical Engineering

Graduate School of UNIST

ULSAN NATIONAL INSTITUTE OF
SCIENCE AND TECHNOLOGY

Design and Analysis of High-*Q* Metasurfaces Using Multipole Expansion

A thesis/dissertation
submitted to the Graduate School of UNIST
in partial fulfillment of the
requirements for the degree of
Master of Science

Nguyen Thi Hai Yen

06/16/2020
Approved by

_____

Advisor
Gangil Byun

ULSAN NATIONAL INSTITUTE OF
SCIENCE AND TECHNOLOGY

Design and Analysis of High-Q Metasurfaces Using Multipole Expansion

Nguyen Thi Hai Yen

This certifies that the thesis of Nguyen Thi Hai Yen is approved.

06/16/2020

signature

_____

Advisor: Prof. Gangil Byun

signature

_____

Prof. Jingook Kim: Thesis Committee Member #1

signature

_____

Prof. Jae-Gon Lee: Thesis Committee Member #2

ULSAN NATIONAL INSTITUTE OF
SCIENCE AND TECHNOLOGY

Abstract

Despite numerous potential advantages of sub-radiative dark modes due to an extremely high quality factor, the practicality still depends on the consistency of excitations for a tight fabrication tolerance. This work proposes a novel approach to adaptive transitions between different dipole moments to allow for consistent excitation of Fano and electric quadrupole resonances that are extremely sensitive to geometric errors. The proposed geometry of each metamolecule consists of four strips printed on a thin dielectric film with four gaps between the strips, and the geometric error is described as structural deformation by adjusting the strip lengths and gap sizes in the vertical direction. In each deformed state, current and magnetic-field distributions are analyzed to interpret operating principles, and multipole moments are calculated based on the multipole expansion using the current distributions. The results demonstrate that the consistent excitation of the electric quadrupole moment is enabled based on a simultaneous transition between toroidal and electric dipole moments, and the Fano resonance is consistently excited by the magnetic-to-electric dipole moment transition. For verification, original and deformed metasurfaces are fabricated, and their transmission and reflection coefficients are measured in a semi-anechoic chamber to experimentally validate the proposed dipole moment transitions. The results confirm that the proposed approach has great potential to bring advances in recent sensing and energy harvesting applications where an extremely high quality factor is essential.

ULSAN NATIONAL INSTITUTE OF
SCIENCE AND TECHNOLOGY

ULSAN NATIONAL INSTITUTE OF SCIENCE AND TECHNOLOGY

Table of Contents

ULSAN NATIONAL INSTITUTE OF
SCIENCE AND TECHNOLOGY

List of Figures

ULSAN NATIONAL INSTITUTE OF
SCIENCE AND TECHNOLOGY

ULSAN NATIONAL INSTITUTE OF
SCIENCE AND TECHNOLOGY

List of Tables

ULSAN NATIONAL INSTITUTE OF
SCIENCE AND TECHNOLOGY

I. Introduction

Resonance with high quality (Q) factors are essential in various applications due to several advantages as illustrated in Figure 1.1: for a sensing purpose, the high Q factor results in a sharp resonance that provides more pronounced spectral shifts with respect to different electromagnetic properties [1]. The high Q resonance is also preferred in wireless power tranfer because it maximizes the power delivered to the load of the receiver by suppressing the stored electromagnetic energy. The sub-radiative behavior of high Q resonance is also benefical to energy harvesting due to its strong localized fields which traps the ambient energy within desired areas [2]. In the radio frequency (RF), most efforts to achieve high Q resonance are considered as macroscopic approachs, which have been made from the circuit and scattered field standpoints as shown in Figures 1.2 (a) and 1.2 (b). However, to produce strong magnetic coupling, which is beneficial to obtain the sub-radiative behavior, bulk designs are inevitable. Despite of the strong magnetic coupling in the optics spectrums, its design freedom is restricted by the short wavelengths. Therefore, simple geometries as in Figure 1.2 (c) are widely utilized. In the microscopic standpoint, which is mostly investigated in optics, the sub-radiative behavior can be analyzed based on the multipole expansion using current distributions induced by electromagnetic waves, since the induced currents can be characterized as a sum of dipole, quadrupole, and higher-order moments [3], [4]. Recent research interests related to these multipole moments are mostly about independent adjustment of their contributions to achieve the high Q resonance [5]–[8]. Note that typical dipolar resonances have broader bandwidths with a lower Q factor due to their radiative behavior, since the Q factor is inversely proportional to the radiation resistance [9]. One of the well-known approaches to a high Q factor is the use of interaction between bright and dark modes, i.e. the Fano resonance [10]–[14]. The Q factor can also be enhanced by inducing two antiparallel dipole moments in a single metamolecule to excite a quadrupole moment, which is sub-radiative due to being a dark mode [15]. However, excitation of the dark mode has been a challenging research area since the destructive interaction occurs when two modes or moments completely cancel each other out with the same magnitude in opposite directions. This implies that the dark-mode excitation is extremely sensitive to geometrical parameters, material properties, and fabrication tolerance. Owing to this sensitivity, most of the previous works are limited to the following: first, most of the theoretical predictions have been established in optical wave spectrums because of stronger microscopic interactions; however, extremely short wavelengths lower the flexibility of structural modifications [16]–[19]. Second, although the structural modifications become more flexible in microwave spectrums due to longer wavelengths [20]–[22], this does not provide any fundamental solution to consistent excitations because it still depends highly on the geometrical parameters.

ULSAN NATIONAL INSTITUTE OF SCIENCE AND TECHNOLOGY

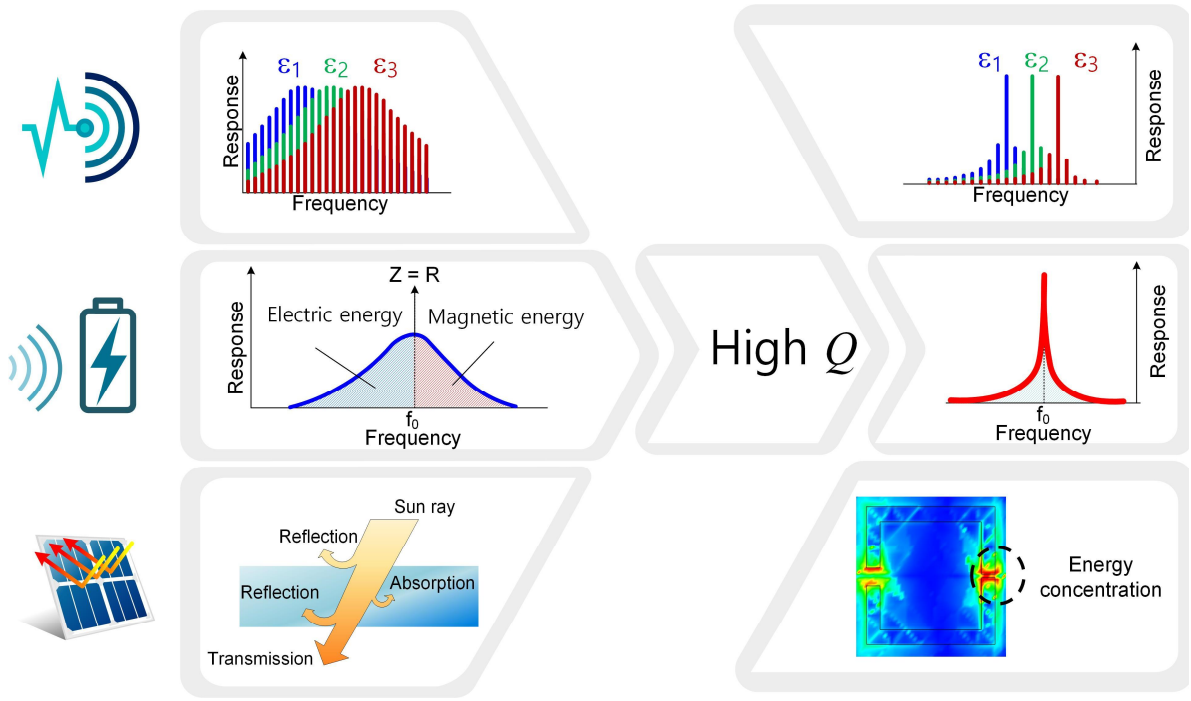

Figure 1.1. Advantages of high Q resonances in various applications.

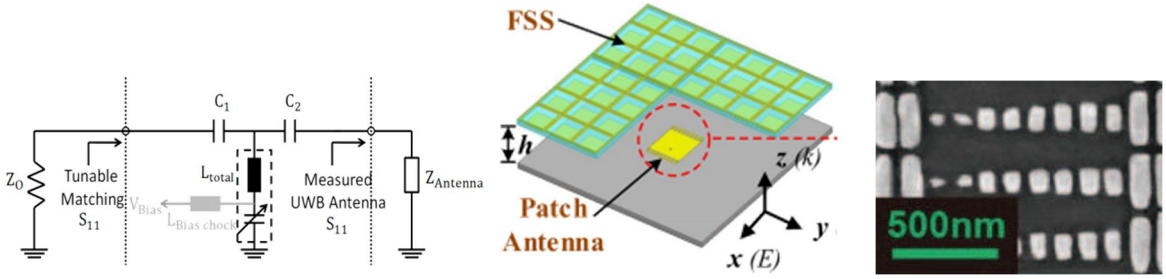

(a) (b) (c)

Figure 1.2. Approaches to high Q resonance: (a) Matching circuit in radio waves [23]; (b) Cavity structure in Microwaves [24], and (c) Nano structure in optics [25].

ULSAN NATIONAL INSTITUTE OF
SCIENCE AND TECHNOLOGY

Here, we introduce a novel approach to geometry-independent excitations of dark modes using adaptive transitions between different dipole moments to maintain consistency in the existence of geometric errors. The proposed approach employs four strips printed on a thin dielectric film to form the shape of two rectangular loops for each metamolecule. One of the novel aspects of the structure compared to previous works is that the gaps between the strips are placed along the horizontal plane to interact with vertically polarized waves. Note that most of the structures reported in previous works [6], [8] place gaps in the vertical plane to achieve the same interaction. The proposed placement of the gaps, in fact, plays a key role to consistently excite two dark modes, herein Fano and electric quadrupole resonances, even when existing considerable geometric errors in metamolecules. This geometry-independent excitation is enabled based on simultaneous transitions between two different dipole moments: toroidal and electric dipole moments for the electric quadrupole and magnetic and electric dipole moments for the Fano resonance. These dipole moment transitions are experimentally demonstrated by defining five deformed states, each of which characterizes different geometric errors. Then, sample metasurfaces are fabricated to measure their frequency responses of transmission and reflection coefficients. We also provide in-depth analyses on the mechanism of toroidal-to-electric and magnetic-to-electric dipole transitions based on the multipole expansion [4] with detailed observations of near field and current distributions. We think that the proposed approach of dipole moment transitions will provide potential breakthroughs in future sensing and energy harvesting applications with a high degree of tolerance against geometric errors. In addition, the proposed concept can be expanded to flexible or stretchable substrates whose frequency responses are easily affected by geometric deformation.

ULSAN NATIONAL INSTITUTE OF
SCIENCE AND TECHNOLOGY

II. Design and Analysis

2.1. Characterization of geometric error

Figure 2.1(a) shows five states of deformed metamolecules representing different geometric errors. The original structure, State 1, is composed of two square loops placed side by side, and these square loops are divided into upper and lower strips by inserting four gaps along the horizontal plane (*z*-*x* plane). The detailed design procedure is provided in the Appendix. It is of importance to adjust gap sizes and their positions for dark-mode excitations in such a way that the geometry becomes asymmetric in both vertical and horizontal planes [26]–[28]. Note that we use the terms 'central' and 'lateral' to specify gap positions according to the distance from the vertical plane (*z*-*y* plane) for ease of explanations. In our design, two lateral gaps are completely symmetric whereas one of the central gaps is slightly enlarged and the other parameters are maintained to be identical for the structural simplicity. To characterize various deformation states, we stretch the geometry in the vertical direction so that the metamolecule shrinks in the horizontal plane with increasing lateral gaps. Thus, the ratio between horizontal and vertical lengths of metamolecules increases from 0.5 to 1.6, as the state index increases. Figures 2.1(b) and 2.1(c) show conceptual illustrations of dipole moment transitions of State 1 and State 5, respectively. The gray arrows indicate electric currents induced on the strips, and these currents generate magnetic and electric dipole moments, as specified by red and blue arrows, respectively. The circulation of magnetic currents produces toroidal dipole moments expressed by green arrows, and the equivalence to the electric quadrupole is specified by using two pairs of positive and negative charges.

ULSAN NATIONAL INSTITUTE OF SCIENCE AND TECHNOLOGY

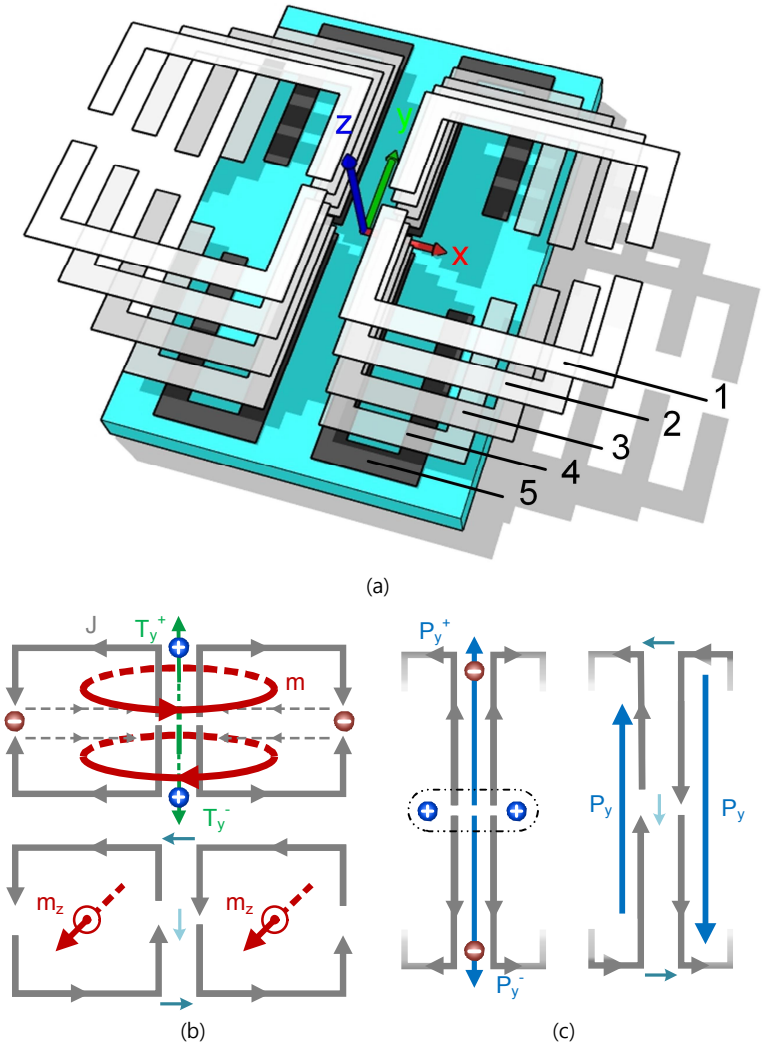

Figure 2.1. (a) Five deformed states denoted by numbers from 1 to 5. Conceptual illustrations of dipole moment transitions between (b) State 1 and (c) State 5 are presented.

ULSAN NATIONAL INSTITUTE OF
SCIENCE AND TECHNOLOGY

Figure 2.2 shows the geometry and its design parameters that are used to define five deformed states whose size of the metamolecule is adjusted by p_x and p_y. Four strips are designed using w_x, w_y, and w_{ms}, and the gaps between the strips are specified by s_c, s_l, and g. Note that s_u plays a key role to break the symmetry in both vertical and horizontal planes that are specified by dash-dot lines. These parameters are tuned for the X-band operation, and detailed values of the five states are listed in Table 1. It is worth noting that the proposed approach to the broken symmetry is distinguished from most of the prior works varying only the gap positions, e.g. [29] and [30], and give more design freedom in terms of current distributions. More specifically, the geometry in [29] has a single central strip that is not separated into left and right, and this restricts the vertical current at the center to point the same direction in either upward or downward. Due to this restriction, the geometry excites a single dark mode of toroidal dipole moment along with two electric dipoles. Although the geometry in [30] has separated strips at the center, there are only central gaps, and the high-order dark mode, herein octupole is excited only as a harmonic resonance. Thus, the resonant frequency of the octupole is three-time higher than that of the magnetic dipole, on the other hand, our design is capable of simultaneously exciting two dark modes within the X band for the five deformed states.

ULSAN NATIONAL INSTITUTE OF SCIENCE AND TECHNOLOGY

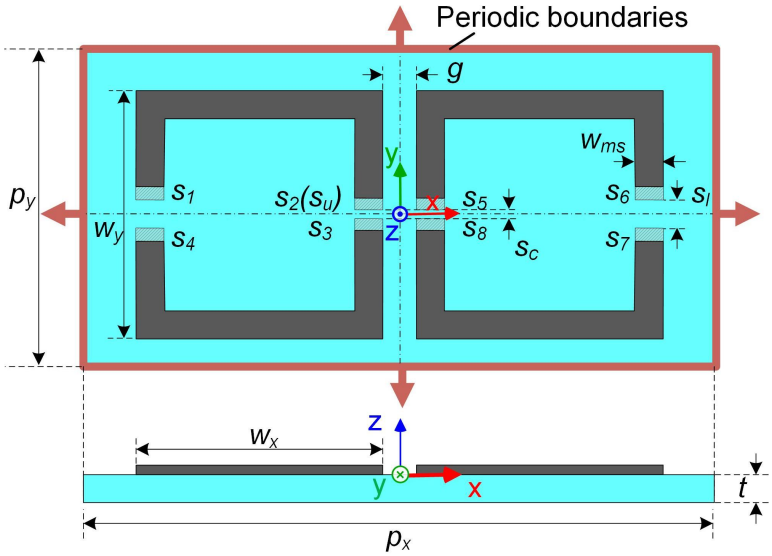

Figure 2.2. Top and side views of a single metamolecule with design parameters and periodic

Table 2.1: Design parameters and their values

Parameters	p_x	p_y	w_x	w_y	s_l	g
State 1	18	9	7	7	0.8	1
State 2	16	10.8625	6	8.8625	2.72	0.94
State 3	14	12.725	5	10.725	4.65	0.88
State 4	12	14.5875	4	12.5875	6.58	0.82
State 5	10	16	3	14.45	8.5	0.75

(s_c = 0.2, s_2 = 0.1, s_1 = s_3 = s_4 = s_5 = s_6 = s_7 = s_8 = 0, w_{ms} = 0.75, and t = 0.12 for all designs (unit: mm))

ULSAN NATIONAL INSTITUTE OF
SCIENCE AND TECHNOLOGY

In our full-wave electromagnetic simulations, the geometry of each metamolecule is modeled as piecewise triangular meshes in *xy*-plane, and the infinite periodic boundary condition is applied in both *x*- and *y*-directions to realize an infinite two-dimensional array. A far-field source is excited along the *z*-axis to be normally incident to the geometry, and the source is linearly polarized with a tilt angle of 0°. The dielectric substrate is modeled using a cuboid with properties of $\varepsilon_r = 2.66$ and $\tan\delta = 0$, and the metallic triangles are assumed as the perfect electric conductor ($\sigma = \infty$) to ignore conduction losses. Note that only the fabricated metasurface is tuned by considering actual material properties, which will be provided in Section 3.1. The simulated data are obtained in a frequency range from 8 GHz to 12 GHz with the minimum interval of 40 kHz, and the triangular meshes are designed to have edge lengths of less than 0.05 λ at 10 GHz, which produces the total number of 756 meshes in State 5.

Figure 2.3 presents transmission and reflection coefficients of the five states for vertically polarized waves along y-axis, and highlighted resonances at dip positions represent excited dark modes: electric quadrupole moment (Q_e) and magnetic dipole moment (M_z), i.e. the Fano resonance. It is worth noting that these dark modes are consistently excited although the structure is stretched in the vertical direction, for example, dark-mode resonances appear at 9.4 GHz (Q_e) and 9.7 GHz (M_z) in State 1, and they still exist at 9.2 GHz (Q_e) and 10.9 GHz (M_z) in State 5. To provide an in-depth analysis on such geometry-independent excitation of sub-radiative dark modes, multipole moments are calculated based on the multipole expansion [4], [32] using the information of electric currents induced on the metallic strips.

ULSAN NATIONAL INSTITUTE OF SCIENCE AND TECHNOLOGY

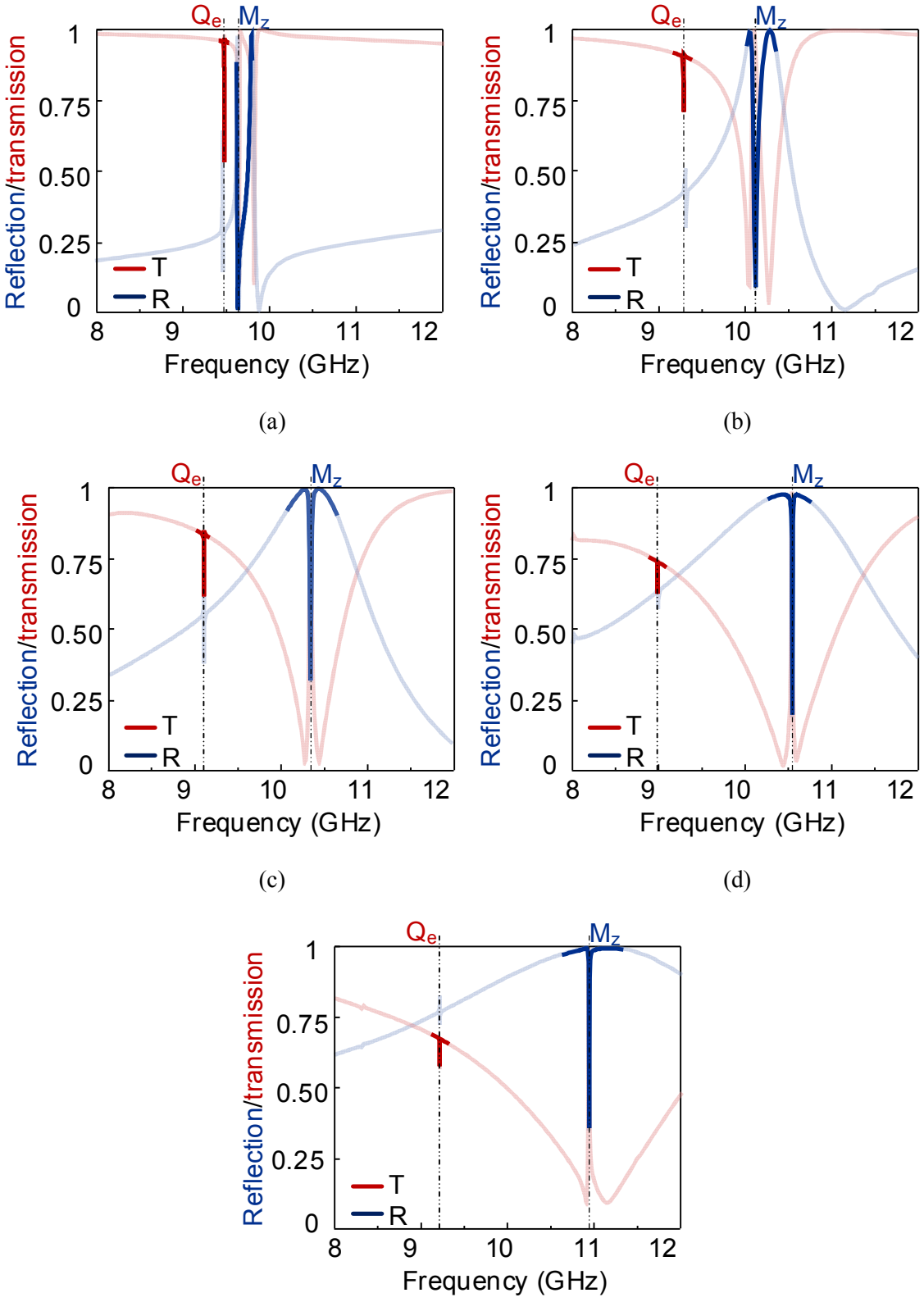

Figure 2.3. Transmission and reflection coefficients of the five states are compared, and *Q* factors of electric quadrupole (Q_e) and Fano (M_z) resonances are greater than 9,250 and 170, respectively. (a) State 1, (b) State 2, (c) State 3, (d) State 4, and (e) State 5.

ULSAN NATIONAL INSTITUTE OF SCIENCE AND TECHNOLOGY

2.2. Analysis.

2.2.1. Multipole Expansion

To calculate multipole moments based on the multipole expansion, we first need to obtain vector electric current density **J** induced on metallic triangular meshes from full-wave electromagnetic simulations. In Cartesian coordinates, the vector components of J_x, J_y, and J_z are exported as raw data to use in the computation of multipole moments using the following equations:

Electric dipole moment:

$$P_y = \frac{1}{i\omega}\int J_y d^3r \tag{1}$$

Magnetic dipole moment:

$$M_z = \frac{1}{2c}\int (\boldsymbol{r}\times\boldsymbol{J})_z d^3r = \frac{1}{2c}\int (yJ_x + xJ_y) d^3r \tag{2}$$

Toroidal dipole moment:

$$\begin{aligned} T_y &= \frac{1}{10c}\int\left[(\boldsymbol{r}\cdot\boldsymbol{J})r_y - 2r^2 J_y\right] d^3r \\ &= \frac{1}{10c}\int\left[\left(xJ_x + yJ_y\right)y - 2\left(x^2+y^2\right)J_y\right] d^3r \end{aligned} \tag{3}$$

Electric quadrupole moment:

$$\begin{aligned} \boldsymbol{Q}_{\alpha\beta} &= \frac{1}{2i\omega}\int\left[r_\alpha J_\beta + r_\beta J_\alpha - \frac{2}{3}(\boldsymbol{r}\cdot\boldsymbol{J})\delta_{\alpha\beta}\right] d^3r \\ &= \frac{1}{2i\omega}\int\left[r_\alpha J_\beta + r_\beta J_\alpha - \frac{2}{3}\left(xJ_x + yJ_y\right)\delta_{\alpha\beta}\right] d^3r \end{aligned} \tag{4}$$

where $\boldsymbol{r}$ is the position vector from the origin to the centroid position of each triangular mesh. ω is the angular frequency, and c is the speed of light. The subscript α and β can be selected as one of coordinate components x, y, and z, and δ represents the Kronecker delta that is equal to unity only for the same coordinate components (and zero otherwise).

Then, the scattering intensity associated with the multipole moments can be calculated using the following equations:

Scattering intensity due to electric dipole moment P_y:

$$I_{P_y} = \frac{2\omega^4 \mid P_y \mid^2}{3c^3} \tag{5}$$

Scattering intensity due to magnetic dipole moment M_z:

ULSAN NATIONAL INSTITUTE OF SCIENCE AND TECHNOLOGY

$$I_{M_z} = \frac{2\omega^4 |M_z|^2}{3c^3} \tag{6}$$

Scattering intensity due to toroidal dipole moment T_y:

$$I_{T_y} = \frac{2\omega^6 |T_y|^2}{3c^5} \tag{7}$$

Scattering intensity due to electric quadrupole moment $Q_{\alpha\beta}$:

$$I_{Q_e} = \frac{\omega^6}{5c^5} \sum |\boldsymbol{Q}_{\alpha\beta}|^2 \tag{8}$$

2.2.2. Analysis based on multipole expansion

Figure 2.4 shows comparisons of multipole moments and transmission coefficients of all states with the geometry of each metamolecule as an in-set figure. In State 1, the electric quadrupole moment (Q_e) has the greatest peak at the first resonance, when the magnetic dipole moment (M_z) is being dominant for the other two resonances. Another interesting phenomenon is that the peaks of the toroidal dipole moment (T_y) are aligned with those of the magnetic dipole moment at 9.4 GHz, 9.6 GHz, and 9.8 GHz. This is because the toroidal dipole moment is induced by two antiparallel magnetic dipole moments, when two square loops of the metamolecule operate as a two-dimensional toroid [33]. In State 2, the first resonance is still associated with the electric quadrupole moment, however, the major contribution of the second and third transmission resonances at 10 GHz and 10.2 GHz is switched to the electric dipole moment. Instead, the remaining magnetic dipole moment at 10 GHz produces a trapped mode, which accompanies to a Fano resonance in reflection coefficients [21]. Note that the average levels of the magnetic and toroidal dipole moments tend to decrease as the state index increases while that of the electric dipole moment shows the opposite trend. As a result, in State 5, the electric dipole moment becomes dominant over a wide frequency range, but, nevertheless, the electric quadrupole and Fano resonances still exist at 9.2 GHz and 10.9 GHz, respectively.

To evaluate the validity of our observation on the transition of multipole moments provided in Figure 2.4, we calculate the scattering intensity associated with P_y, T_y, M_z, and Q_e in the backward ($+z$) direction, and their sum is normalized by the incident amplitude [3]. Figure 2.5 presents the calculated sum of scattering contributions in comparison with the simulated reflection coefficients that are identical to Figure 2.3, but in log-scale. The results confirm that multipole moments calculated using the currents in the metallic parts make dominant contributions, and the involvement of substrate displacement currents can be negligibe.

ULSAN NATIONAL INSTITUTE OF SCIENCE AND TECHNOLOGY

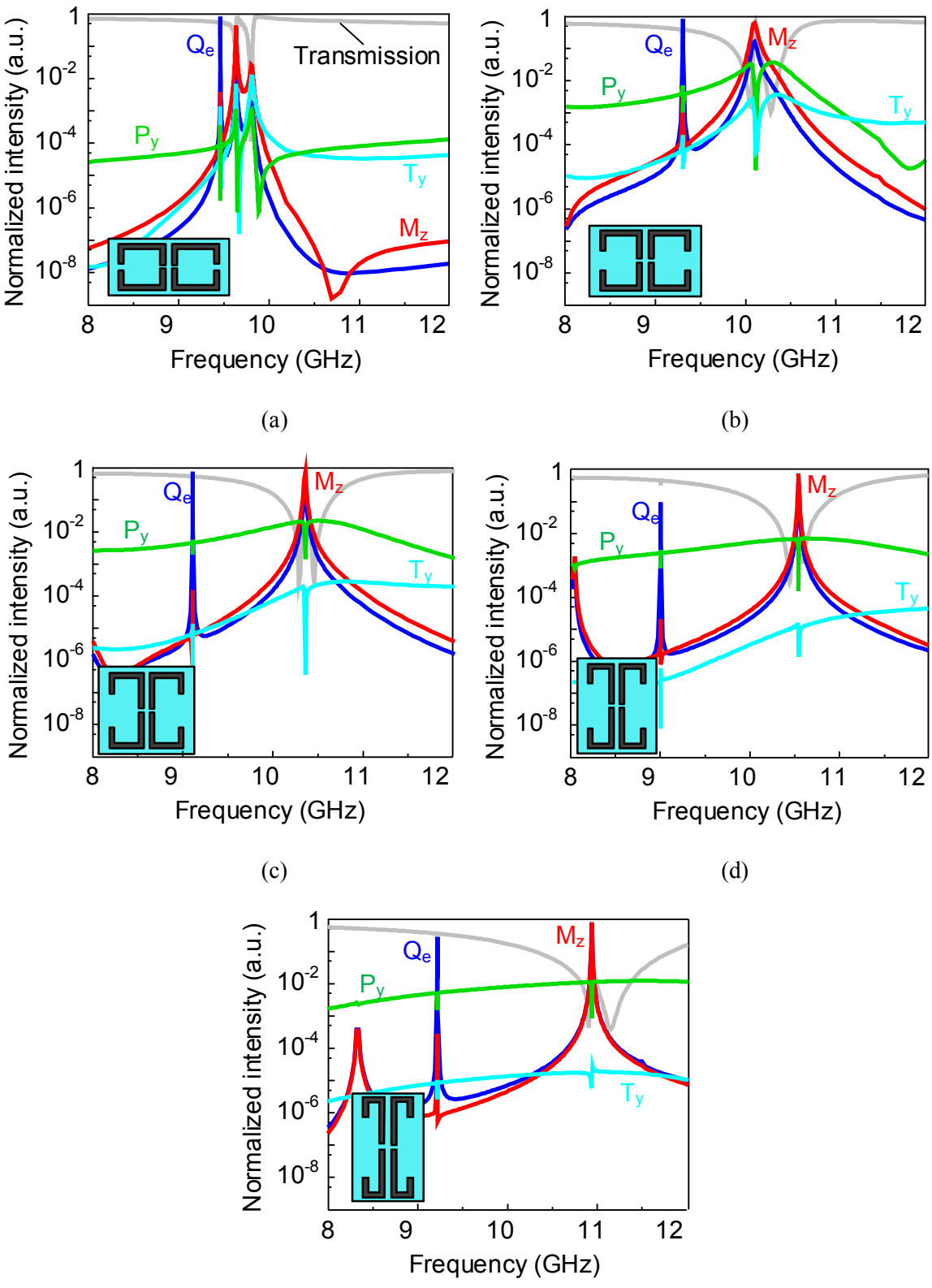

Figure 2.4. Normalized scattering intensity of electric dipole (P_y), toroidal dipole (T_y), magnetic dipole (M_z), and electric quadrupole (Q_e) are calculated by the multipole expansion using current distributions in (a) State 1, (b) State 2, (c) State 3, (d) State 4, and (e) State 5

ULSAN NATIONAL INSTITUTE OF SCIENCE AND TECHNOLOGY

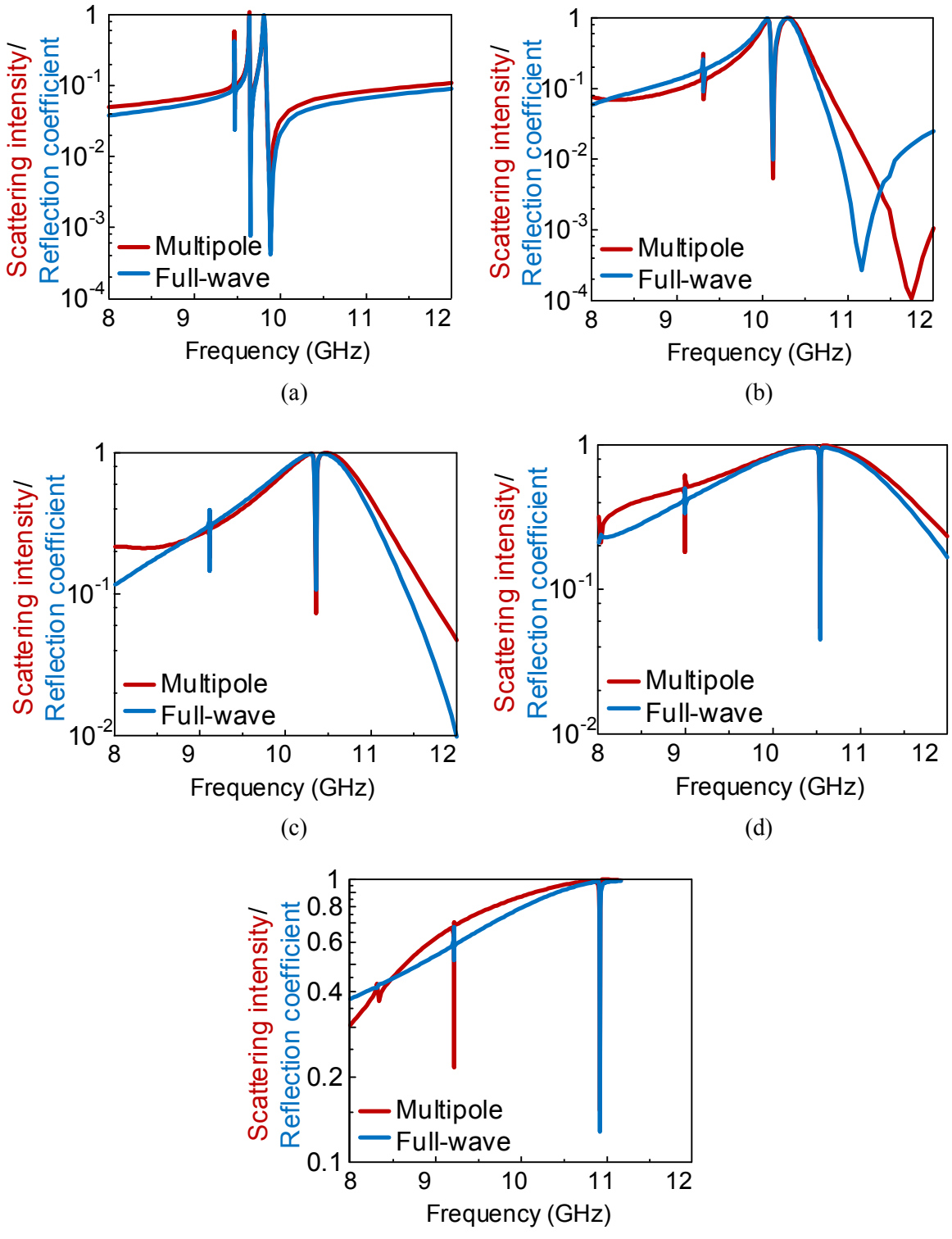

Figure 2.5. Comparison of simulated reflection coefficients with the sum of scattering intensity by electric dipole (P_y), toroidal dipole (T_y), magnetic dipole (M_z), and electric quadrupole (Q_e) moments obtained from currents in metallic parts: (a) State 1, (b) State 2, (c) State 3, (d) State 4, and (e) State 5.

ULSAN NATIONAL INSTITUTE OF
SCIENCE AND TECHNOLOGY

2.2.2.1. Toroidal-to-electric dipole transition

Figure 2.6 shows absolute values of electric currents with arrows to specify directions of the currents and magnetic fields at the electric quadrupole resonance. In State 1, each strip forms a circulation of electric currents, thus, two upper strips induce magnetic fields toward opposite directions. This is equivalent to the field distributions of a two-dimensional toroid placed in *x*-*y* plane, which produces a toroidal dipole moment in +*y*-direction. In a similar manner, current distributions of two lower strips make another toroidal dipole moment in the opposite direction, and these antiparallel toroidal dipole moments excite the electric quadrupole moment. However, as the geometry is stretched in the vertical direction, the current circulation of each strip becomes weaker due to a reduced length in *x*-direction, so the toroidal dipole moment diminishes together (Figure 2.1(c)). Alternatively, the upper and lower strips induce linearly oscillating currents toward opposite directions, which results in two antiparallel electric dipole moments enabling the excitation of electric quadrupole moments. To more thoroughly observe this toroidal-to-electric dipole transition, the strengths of scattering intensity in the far-field zone for toroidal and electric dipole moments as well as their phases are separately calculated for upper and lower strips as shown in Figures 2.7(a) and 2.7(b). In State 1, two toroidal dipole moments have a phase difference of 180° with similar magnitudes of about 10^{-2}, and they are greater than the electric dipole moments by a factor of 10^{2}. Due to the reduced current circulation, the toroidal dipole moment shows a decreasing trend for both upper and lower strips, on the contrary, the electric dipole moment becomes stronger for a larger state index. Thus, the intensity ratio of the electric dipole to toroidal dipole moments tends to increase as indicated by a red line, and this dipole moment transition provides consistent excitation by accompanying with the steady phase difference of about 180°.

ULSAN NATIONAL INSTITUTE OF
SCIENCE AND TECHNOLOGY

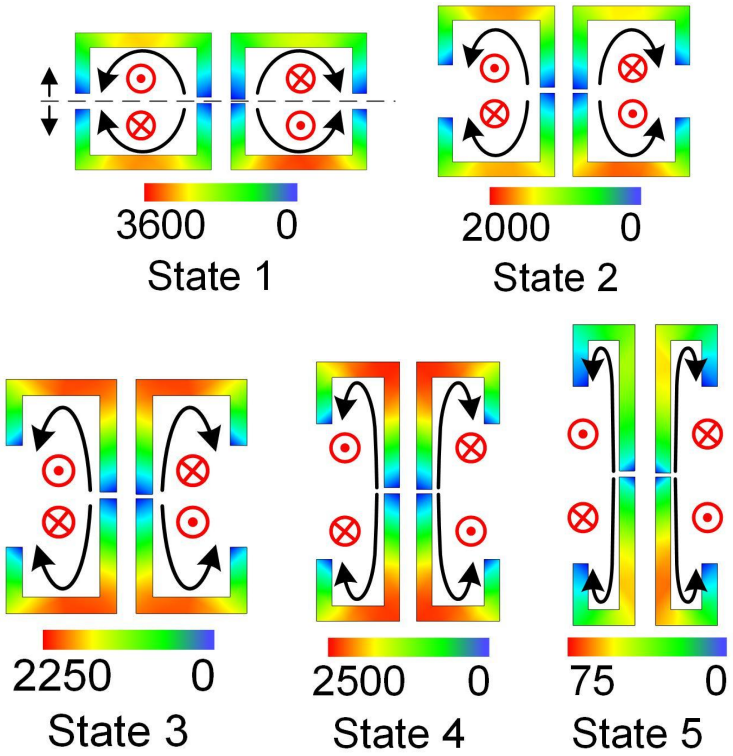

Figure 2.6. Distributions of surface currents induced on the strips in five states (unit: mA). The black and red arrows illustrate the instantaneous directions of electric and magnetic current densities at *wt* = 0°, respectively, for the electric quadrupole resonance.

ULSAN NATIONAL INSTITUTE OF SCIENCE AND TECHNOLOGY

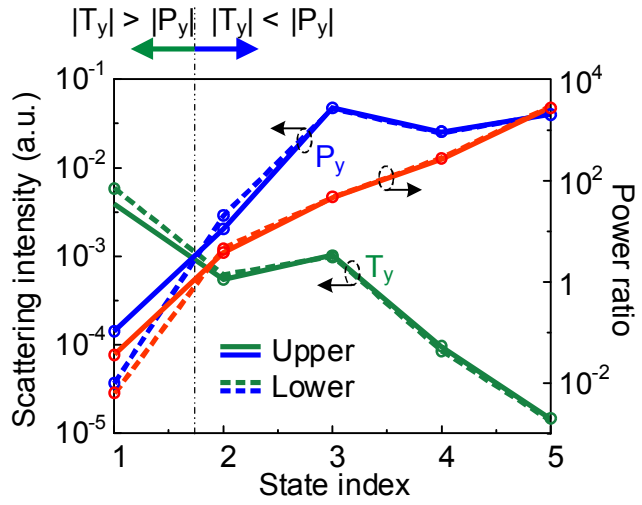

(a)

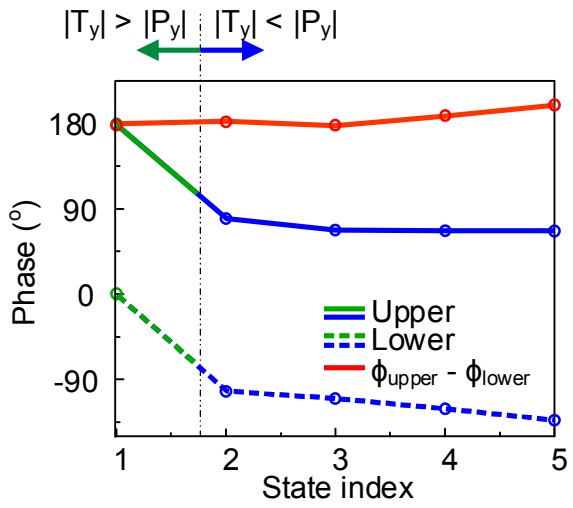

(b)

Figure 2.7. (a) The scattering intensity for electric (blue) and toroidal (green) dipole moments induced on upper (solid) and lower (dashed) strips. The red lines express the amplitude ratio of electric dipole to toroidal dipole moments. (b) Phase variations of dominant dipole moments with

ULSAN NATIONAL INSTITUTE OF
SCIENCE AND TECHNOLOGY

2.2.2.2. Consistent excitation of Fano resonance

Figure 2.8 shows distributions of electric currents in absolute values at three resonant frequencies for State 1 and State 5. The terms 'T_1' and 'T_2' represent the second and third resonant dips of the transmission in Figure 2.3, and 'R' indicates a dip of the reflection between T_1 and T_2, which is the Fano resonance. Note that the square loop of State 1 induces a circulation of electric currents, which produces the magnetic dipole moment (Figure 2.1(b)), and each side of the strips in State 5 constructs the electric dipole moment in the vertical direction (Figure 2.1(c)). In both states, only the strips on the right-hand side induce strong currents at T_1, and those on the left-hand side become active at T_2. Consequently, current magnitudes on the right and left-hand sides reach the equality at R, which is also known as a trapped mode having the sub-radiative behavior. Figure 2.9 presents variations of scattering intensity for electric and magnetic dipole moments calculated from current distributions of the strips in the right- and left-hand sides, separately. The scattering intensity of the magnetic dipole moment is dominant at both transmission resonances in State 1, and they are 100 times greater than those of the electric dipole moments. Although the contribution of magnetic dipole moments decreases due to the reduced circulation in a larger state index, the Fano resonance R still remains because of raised electric dipole moments, which results in the increasing trend of the intensity ratio specified by red lines.

ULSAN NATIONAL INSTITUTE OF SCIENCE AND TECHNOLOGY

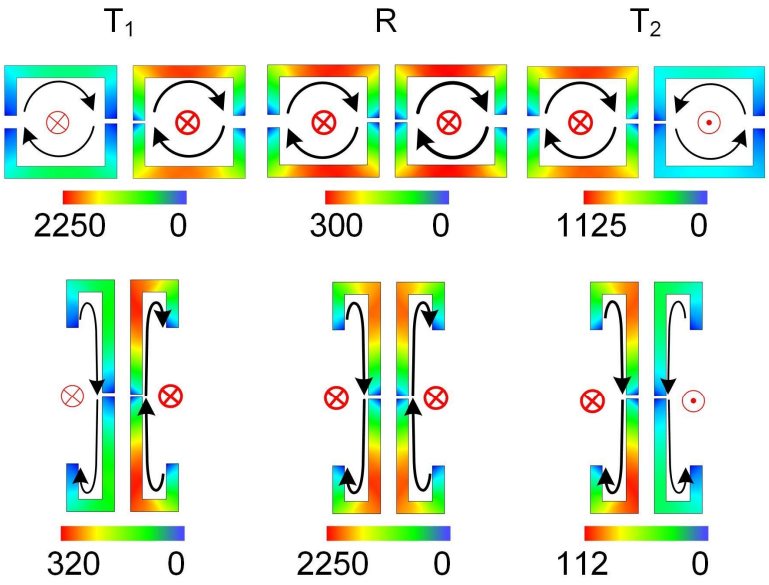

Figure 2.8. Distributions of surface currents in State 1 and State 5 at the second (T_1) and third (T_2) resonances in transmission coefficients and the Fano resonance (R) in reflection coefficients (unit:

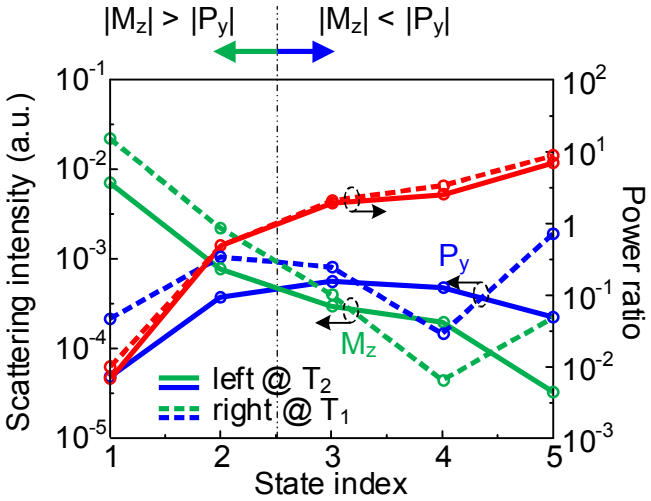

Figure 2.9. The scattering intensity of electric (blue) and magnetic (green) dipole moments induced on the right (dashed) and left (solid) sides at T_1 and T_2 with their ratios (red).

ULSAN NATIONAL INSTITUTE OF
SCIENCE AND TECHNOLOGY

III. Experiments

3.1. Fabrication and measurement

It is now experimentally demonstrated if the geometries in State 1 (original) and State 5 (deformed) produce the two dark modes of electric quadrupole and Fano resonances. To employ more realistic conditions of a real metal and a lossy dielectric material, design parameters are tuned for the actual properties: RT/Duroid 5880 ($\varepsilon_r = 2.2$, $\tan\delta = 0.001$) and copper ($\sigma = 5.8 \times 10^7$), as listed in Table 2. The sample metasurfaces are fabricated by a wet etching process on a thin dielectric film with the overall dimension of 237 mm × 237 mm, and photographs of the fabricated metasurfaces are shown in Figure 3.1.

Figure 3.2 shows detailed measurement setup with a sample holder that is used to make the fabricated metasurface flat, since the substrate is flexible due to the 0.12-mm thickness. Two X-band horn antennas are connected to a network analyzer (Model: N5242A PNA-X) through two coaxial cables, and the interval between each antenna and the metasurface is maintained to be 25 cm ($\geq 10\lambda$ at 12 GHz) for far-field conditions with plane wavefronts. To minimize the effect of ground reflections, the antennas and the sample holder are placed on the top of a Styrofoam cuboid with the overall size of 90 cm (width) × 90 cm (depth) × 60 cm (height), and reflection and transmission coefficients are obtained from measured scattering parameters. To compensate for the space loss of the given environment, first, we measure two-port scattering parameters without the fabricated metasurface and save as free-space data. Then, we conduct another measurement with the fabricated metasurface and subtract the free-space results to get pure frequency responses caused by the metasurface under test. Note that the total of 32,001 frequency points is measured for an increment of 125 kHz in the frequency range from 10 GHz to 14 GHz to clearly detect the resonances with such high Q factors.

ULSAN NATIONAL INSTITUTE OF SCIENCE AND TECHNOLOGY

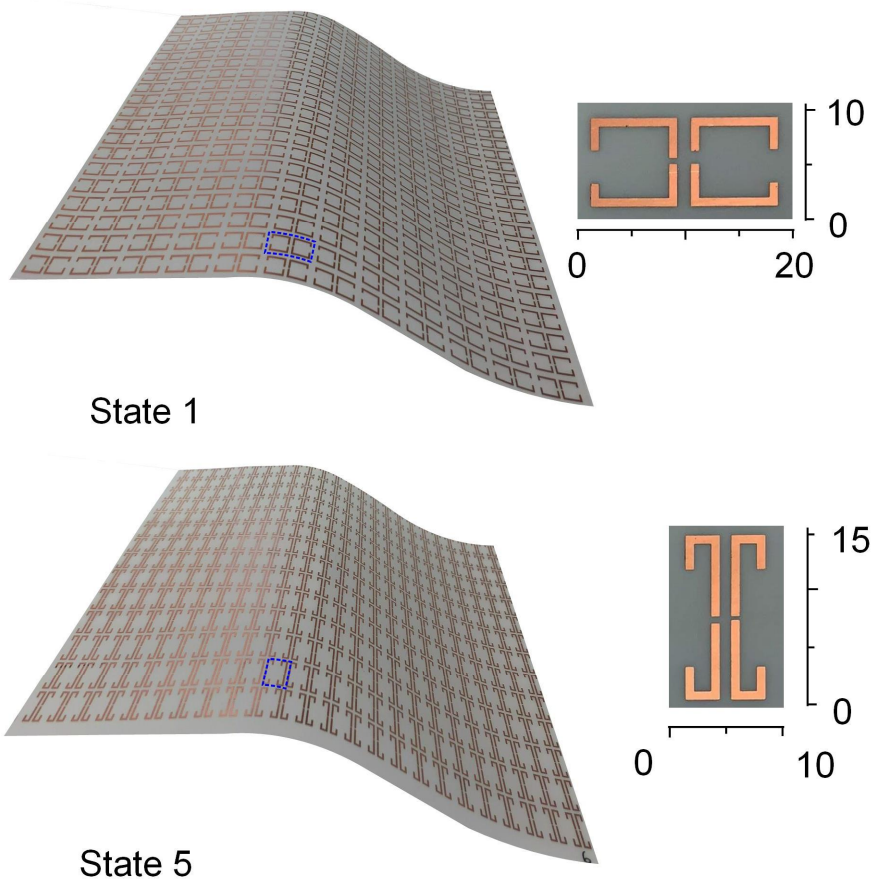

Figure 3.1. Photographs of the fabricated metasurfaces in State 1 (upper) and State 5 (lower). The inset figures show magnified views of the fabricated metamolecules with scale bars (unit: mm).

Table 3.1: Design parameters of fabricated metasurfaces

Parameters	p_x	p_y	w_x	w_y
State 1	19.6	10.3	7.8	7.8
State 5	10	16	3	14.5

Parameters	g	s_2	s_4	s_5	s_7
State 1	1.2	0.2	0.8	0.8	0.8
State 5	0.75	0.8	0	0	0

($s_c = 0.3$, $s_1 = s_3 = s_6 = s_8 = 0$, $w_{ms} = 0.75$, and $t = 0.12$ for all designs (unit: mm))

ULSAN NATIONAL INSTITUTE OF
SCIENCE AND TECHNOLOGY

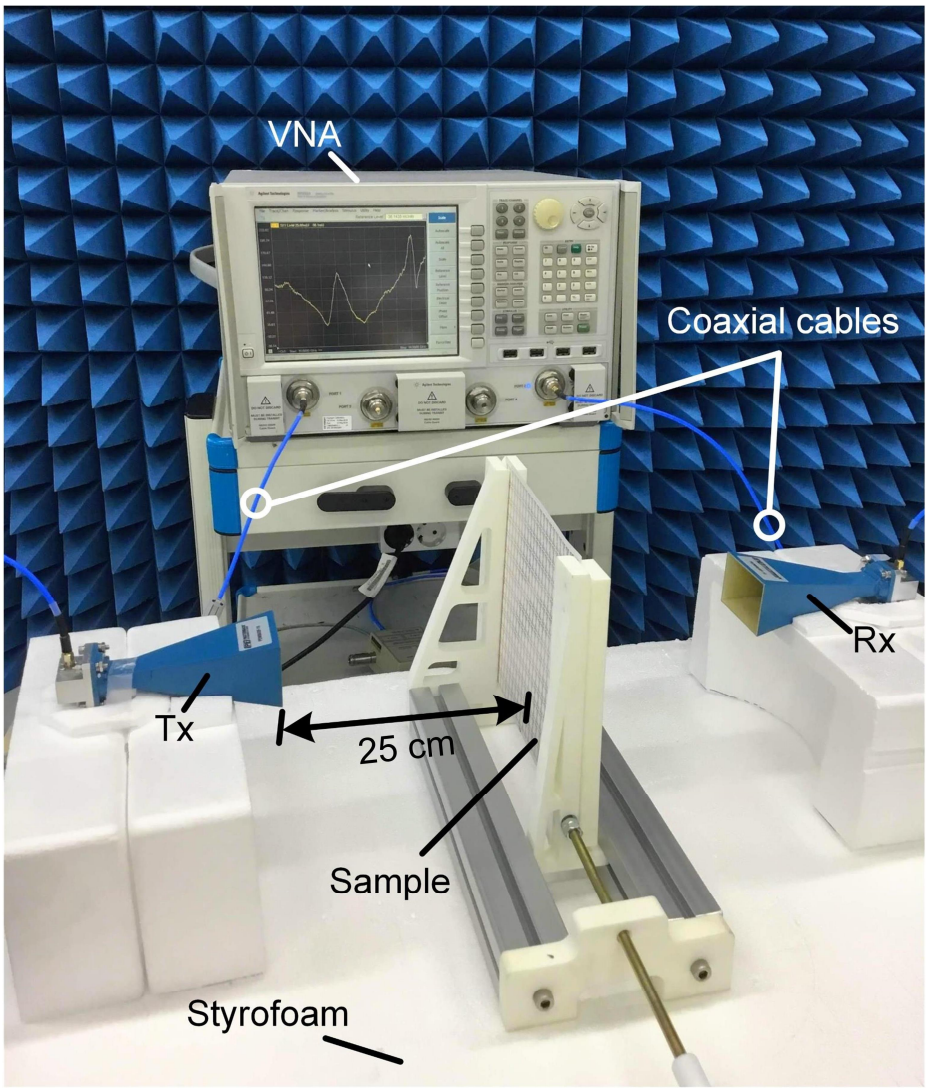

Figure 3.2. Measurement setup: reflection and transmission coefficients of the fabricated metasurface are calculated from measured S_{11} and S_{21}, respectively, by compensating for the space loss.

ULSAN NATIONAL INSTITUTE OF
SCIENCE AND TECHNOLOGY

3.2. Experimental demonstration

Figures 3.3(a) and 3.3(b) present measured transmission and reflection coefficients in comparison with simulated results in State 1 and State 5, respectively. For each state, two transmission resonances are specified by I and III, the Fano resonance of the trapped mode is indicated by II, and the electric quadrupole resonance is IV. We can verify that the measured data agree well with the simulated results, and the major cause of reduced Q factors is due to the finite conductivity and the dielectric loss of the substrate. Figure 3.4 shows variations of multipole moments and current distributions in State 1, and those in State 5 are shown in Figure 3.5. As can be seen, the magnetic dipole moments are being dominant at II, and the peak of the electric quadrupole moments are associated with resonances IV. The strips on the right- and left-hand sides induce strong currents at I and III, respectively, and transitional current distributions are observed at II. Two antiparallel toroidal dipole moments in State 1 and electric dipole moments in State 5 are generated by upper and lower strips at IV, and their destructive interferences excite the electric quadrupole moment as discussed in the previous section.

ULSAN NATIONAL INSTITUTE OF
SCIENCE AND TECHNOLOGY

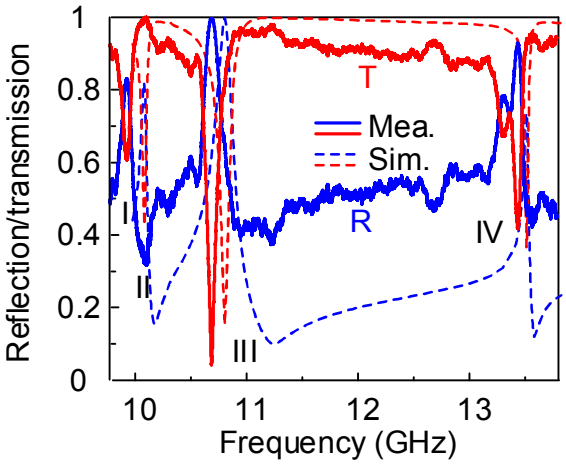

(a)

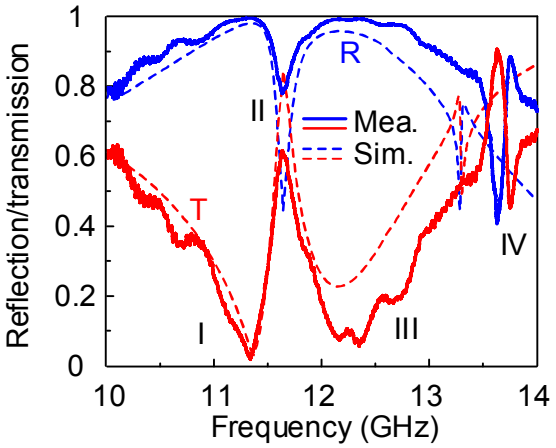

(b)

Figure 3.3. Measured reflection (R, blue) and transmission (T, red) coefficients in comparison with simulation (dashed) of (a) State 1 and (b) State 5.

ULSAN NATIONAL INSTITUTE OF SCIENCE AND TECHNOLOGY

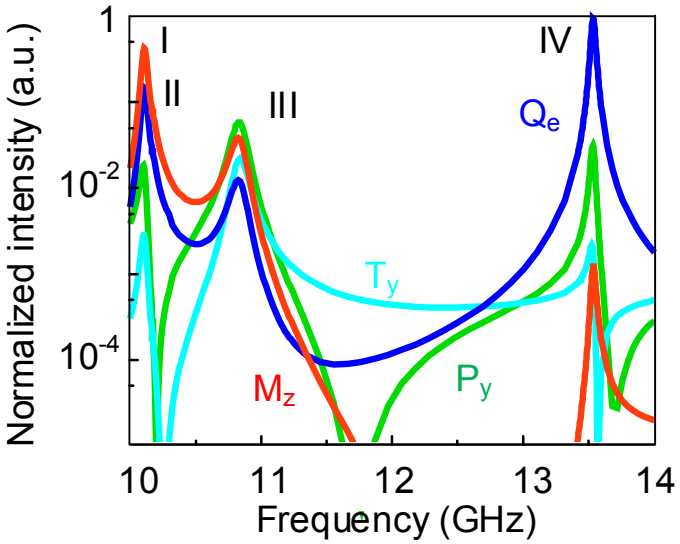

(a)

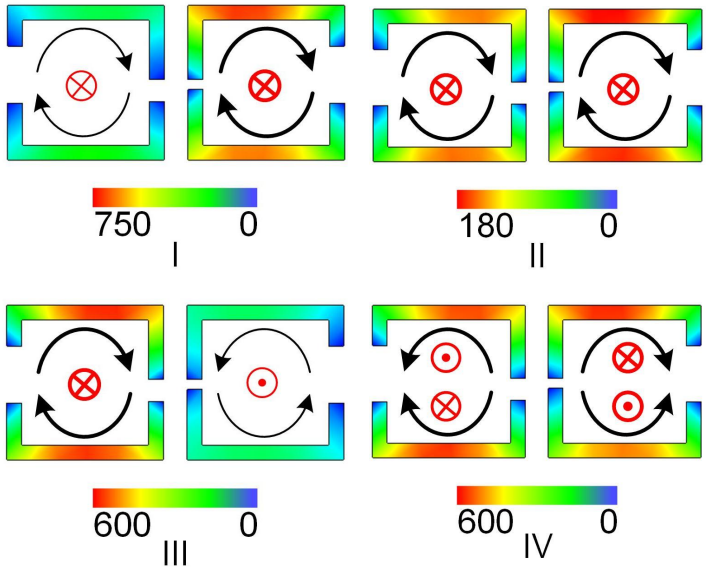

(b)

Figure 3.4. (a) The scattering intensity of multipole moments over the frequency range and (b) Surface current distributions with instantaneous directions of electric and magnetic current densities in State 1.

ULSAN NATIONAL INSTITUTE OF SCIENCE AND TECHNOLOGY

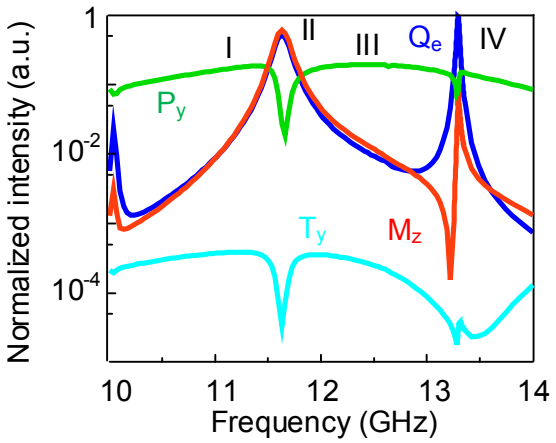

(a)

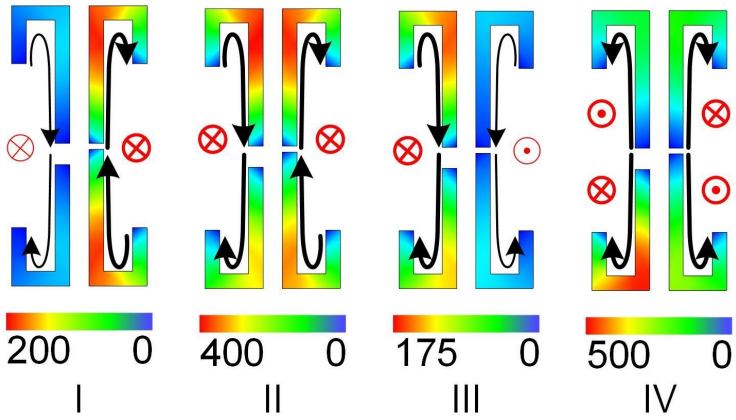

(b)

Figure 3.5. (a) The scattering intensity of multipole moments over the frequency range and (b) Surface current distributions with instantaneous directions of electric and magnetic current densities in State 5.

ULSAN NATIONAL INSTITUTE OF
SCIENCE AND TECHNOLOGY

3.3. Analysis on structural deformation

The validity of the proposed structure is further evaluated by performing additional analyses using a numerical software that calculates geometrical deformations when a tensile strength is applied [34]. Note that the tensile strength is assumed as 6.5 MPa, and the material properties are selected from the library of the software to stretch the substrate with the given strength. Details of our validation process are as follows:

(1) We model the geometry of State 3 in the software and apply the tensile strength at the upper and right edges, separately. Different tensions of 125 N and 250 N at the right edge lead the geometry of State 3 to that of State 2 and State 1, respectively, while the tensions in the horizontal direction produce State 4 and State 5.

ULSAN NATIONAL INSTITUTE OF
SCIENCE AND TECHNOLOGY

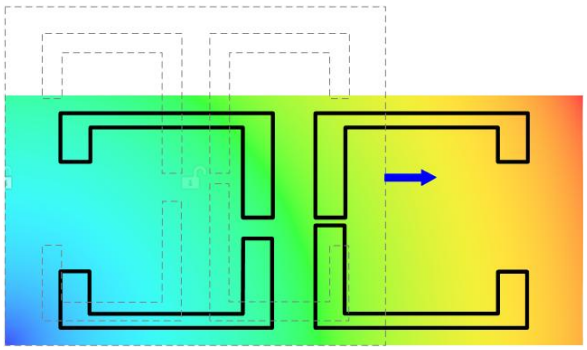

(a)

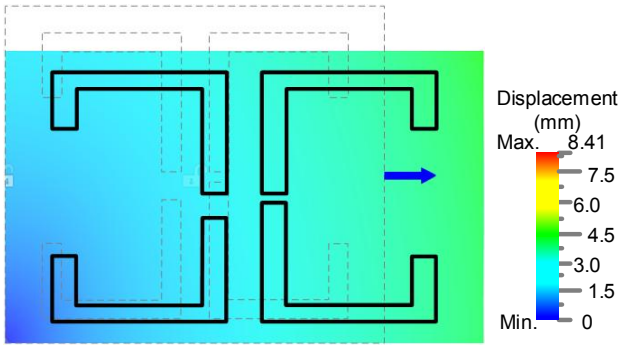

(b)

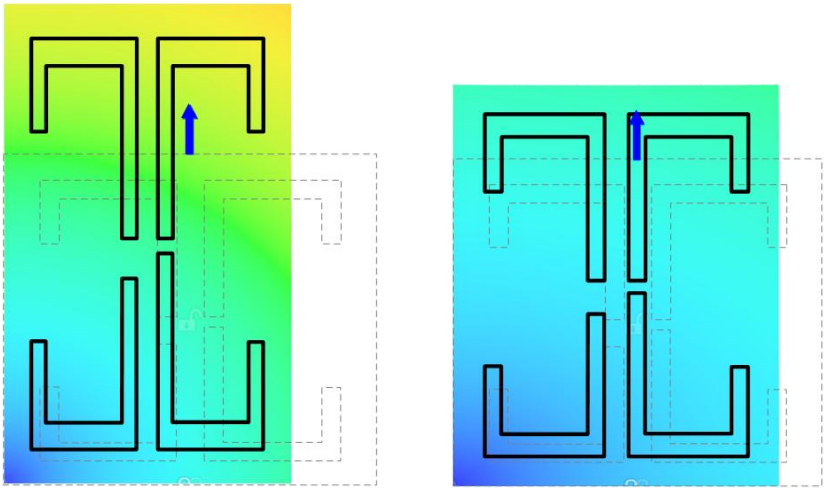

(c) (d)

Figure 3.6. The displacement of geometries due to the tensile strength is specified by colors, and the original geometry of State 3 is indicated by dashed lines. The strength is adjusted to mimic each unit cell's size of (a) State 1, (b) State 2, (c) State 4, and (d) State 5.

ULSAN NATIONAL INSTITUTE OF
SCIENCE AND TECHNOLOGY

(2) The simulation provides displacements of the geometry, such as strip widths and substrate thicknesses, due to the tension, as shown in Figure 3.6. Then, the displacements of geometrical parameters are exported to full-wave electromagnetic simulations to replicate the deformation.

(3) To account for the change of conductivity, i.e. surface resistance, we use the data provided in [31] for describing the stretching effect. For example, State 3 has a conductivity of 2×10^6 S/m at no strain, and the conductivity is reduced to 0.9×10^6 S/m as the strength increases.

Figure 3.7 shows variations of reflection coefficients due to the deformation. Although the dark-mode resonances become less obvious with the reduced conductivity, the proposed geometry is still capable of exciting dark modes for all states of deformations. This implies that the proposed design is valid to excite dark modes under deformations when the conductivity is maintained.

ULSAN NATIONAL INSTITUTE OF SCIENCE AND TECHNOLOGY

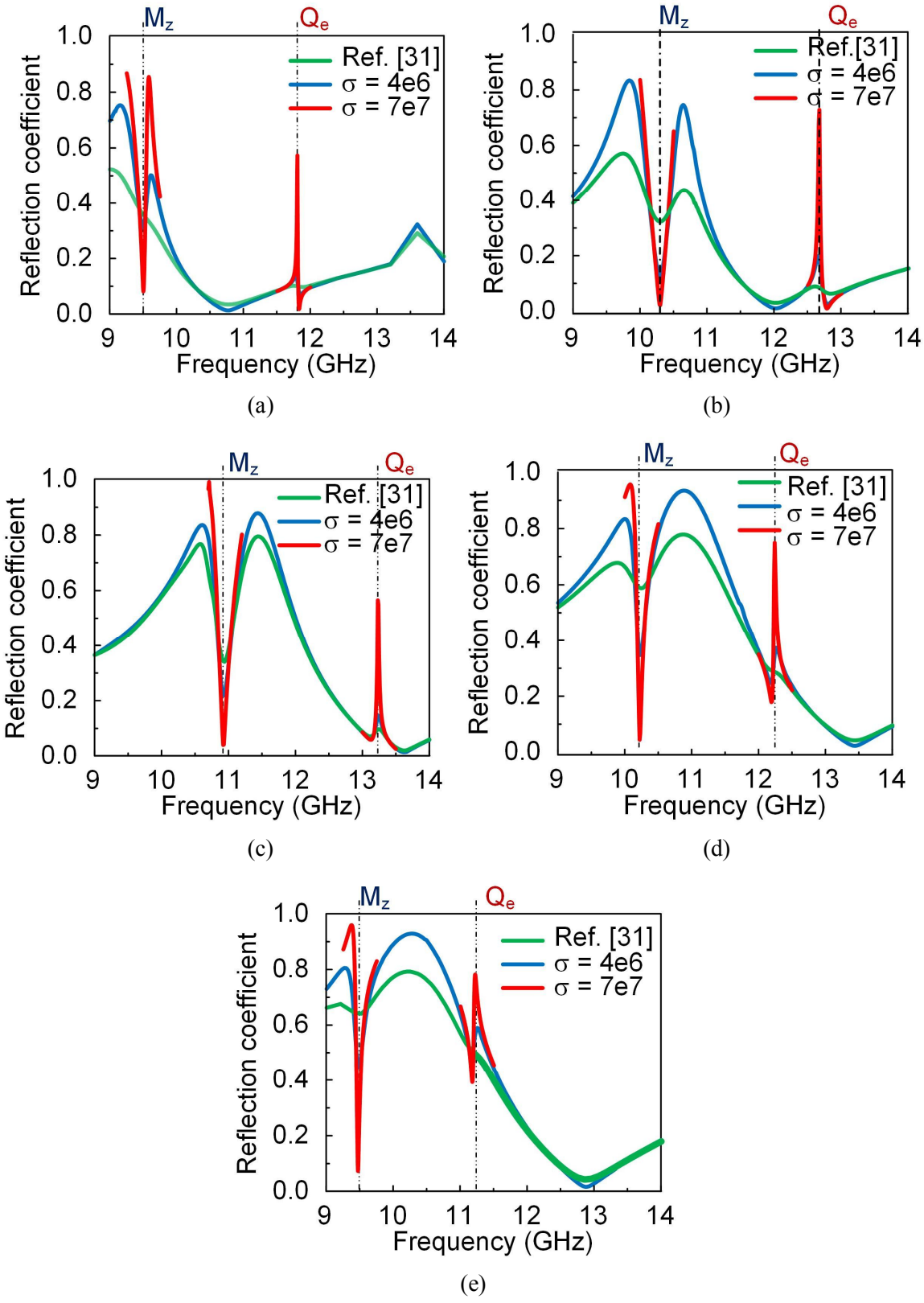

Figure 3.7. Variations of reflection coefficients in the existence of geometrical deformation. The red, blue, and green lines indicate results when applying different conductivity of $\sigma = 7\times 10^7$, $\sigma = 4\times 10^6$, and $\sigma \leq 2\times 10^6$ [31], respectively. (a) State 1, (b) State 2, (c) State 3, (d) State 4, and (e) State 5.

ULSAN NATIONAL INSTITUTE OF
SCIENCE AND TECHNOLOGY

IV. Conclusion

The adaptive transitions between different dipole moments have been explored to demonstrate geometry-independent excitations of dark modes from various standpoints: multipole expansion, reflection and transmission coefficients, and distributions of electric and magnetic current densities. The transition between toroidal and electric dipole moments provided consistent excitations of electric quadrupole moments with the Q factor of greater than 9,250, and the Fano resonance continuously appeared based on the magnetic-to-electric dipole moment transition with the Q factor of greater than 170 in the five deformed states. The feasibility of the proposed approach was further verified using the fabricated metasurfaces, and their reflection and transmission coefficients were measured in the semi-anechoic chamber. The measure results showed that the Fano resonance exists at 10.11 GHz and 11.84 GHz as a trapped mode in State 1 and State 5, respectively, and the electric quadrupole resonance appears at 13.45 GHz and 13.75 GHz. The measured Q factors were 63 (48) and 168 (105) for Fano and electric quadrupole resonances in State 1 (State 5), respectively, and this reduction was mainly caused by the finite conductivity of the metallic strips and the dielectric loss of the film. We believe that the proposed idea will play a key role in making the use of sub-radiative dark modes more practical. In addition, it also has great potential to be expanded for future sensor technologies that utilize stretchable or flexible substrates, which will be our future topics.

ULSAN NATIONAL INSTITUTE OF
SCIENCE AND TECHNOLOGY

REFERENCES

[1] F. Hao, Y. Sonnefraud, P. V. Dorpe, S. A. Maier, N. J. Halas, and P. Nordlander, "Symmetry Breaking in Plasmonic Nanocavities: Subradiant LSPR Sensing and a Tunable Fano Resonance," *Nano Lett.*, vol. 8, no. 11, pp. 3983-3988, Oct. 2008.

[2] C. Fowler and J. Zhou. (2017). A metamaterial-inspired approach to RF energy harvesting. [Online]. Available: https://arxiv.org/abs/1705.07718

[3] V. Savinov, V. A. Fedotov, and N. I. Zheludev, "Toroidal dipolar excitation and macroscopic electromagnetic properties of metamaterials," *Phys. Rev. B*, vol. 89, no. 20, pp. 205112, May 2014

[4] E. V. Tkalya, "Spontaneous electric multipole emission in a condensed medium and toroidal moments," *Phys. Rev. A*, vol. 65, no. 2, pp. 022504, Jan. 2002.

[5] A. A. Basharin, V. Chuguevsky, N. Volsky, M. Kafesaki, and E. N. Economou, "Extremely high Q-factor metamaterials due to anapole excitation," *Phys. Rev. B*, vol. 95, pp. 035104, Jan. 2017.

[6] M. Gupta and R. Singh, "Toroidal versus Fano resonances in high Q planar THz metamaterials," *Adv. Opt. Mater.*, vol. 4, no. 12, pp. 2119-2125, Sep. 2016.

[7] Y. Fan, F. Zhang, N. H. Shen, Q. Fu, Z. Wei, H. Li, and C. M. Soukoulis, "Achieving a high- Q response in metamaterials by manipulating the toroidal excitations," *Phys. Rev. A*, vol. 97, no. 3, pp. 033816, 2018.

[8] S. Han, M. Gupta, L. Cong, Y. K. Srivastava, and R. Singh, "Toroidal and magnetic Fano resonances in planar THz metamaterials," *J. Appl. Phys.*, vol. 122, no. 11, pp. 113105, Sep. 2017.

[9] M. Gustafsson, M. Capek, and K. Schab, "Tradeoff between antenna efficiency and q-factor," *IEEE Trans. Antennas Propag.*, vol. 67, no. 4, pp. 2482-2493, Jan. 2019.

[10] W. X. Lim, M. Manjappa, P. Pitchappa, and R. Singh, "Shaping high-Q planar fano resonant metamaterials toward futuristic technologies," *Adv. Opt. Mater.*, vol. 6, no. 19, pp. 1800502, Jul. 2018.

[11] Q. Li, L. Cong, R. Singh, N. Xu, W. Cao, X. Zhang, Z. Tian, L. Du, J. Han, and W. Zhang, "Monolayer graphene sensing enabled by the strong Fano-resonant metasurface," *Nanoscale*, vol. 8, no. 39, pp. 17278-17284, Sep. 2016.

[12] Q. Xie, G. X. Dong, B. X. Wang, and W. Q. Huang, "High-Q fano resonance in terahertz frequency based on an asymmetric metamaterial resonator," *Nanoscale Res. Lett.*, vol. 13, pp. 294, Sep. 2018.

[13] V. A. Fedotov, J. Wallauer, M. Walther, M. Perino, N. Papasimakis, and N. I. Zheludev, "Wavevector selective metasurfaces and tunnel vision filters," *Light Sci. Appl.*, vol. 4, pp. e306, Jul. 2015.

[14] R. Singh, W. Cao, I. A. Naib, L. Cong, W. Withayachumnankul, and W. Zhang, "Ultrasensitive terahertz sensing with high-Q Fano resonances in metasurfaces," *Appl. Phys. Lett.*, vol. 105, no. 17, pp. 171101, Aug. 2014.

ULSAN NATIONAL INSTITUTE OF SCIENCE AND TECHNOLOGY

[15] N. Liu, M. Hentschel, T. Weiss, A. P. Alivisatos, and H. Giessen, "Three-dimensional plasmon rulers," *Science*, vol. 332, no. 6036, pp. 1407-1410, Jun. 2011.

[16] S. Wu, J. Liu, L. Zhou, Q. Wang, Y. Zhang, G. Wang, and Y. Zhu, "Electric quadrupole excitation in surface plasmon resonance of metallic composite nanohole arrays," *Appl. Phys. Lett.*, vol. 99, no. 14, pp. 141104, Aug. 2011.

[17] N. E. J. Omaghali, V. Tkachenko, A. Andreone, and G. Abbate, "Optical sensing using dark mode excitation in an asymmetric dimer metamaterial," *Sensors*, vol. 14, no. 1, pp. 272-282, Dec. 2014.

[18] S. Panaro, F. de Angelis, and A. Toma, "Dark and bright mode hybridization: From electric to magnetic Fano resonances," *Opt. Lasers Eng.*, vol. 76, pp. 64-69, Jan. 2016.

[19] N. Liu, T. Weiss, M. Mesch, L. Langguth, U. Eigenthaler, M. Hirscher, C. Sönnichsen, H. Giessen, "Planar metamaterial analogue of electromagnetically induced transparency for plasmonic sensing," *Nano Lett.*, vol. 10, no. 4, pp. 1103-1107, Apr. 2010.

[20] A. Dhouibi, S. N. Burokur, A. Lupu, A. Lustrac, and A. Priou, "Excitation of trapped modes from a metasurface composed of only Z-shaped meta-atoms," *Appl. Phys. Lett.*, vol. 103, no. 18, pp. 184103, Oct. 2013.

[21] V. A. Fedotov, M. Rose, S. L. Prosvirnin, N. Papasimakis, and N. I. Zheludev, "Sharp trapped-mode resonances in planar metamaterials with a broken structural symmetry," *Phys. Rev. Lett.*, vol. 99, no. 14, pp. 147401, Oct. 2007.

[22] E. Bochkova, S. N. Burokur, A. Lustrac, and A. Lupu, "Direct dark modes excitation in bi-layered enantiomeric atoms-based metasurface through symmetry matching," *Opt Lett.*, vol. 41, no. 2, pp. 412-415, Jan. 2016.

[23] C. S. Lee and C. L. Yang, "Matching Network Using One Control Element for Widely Tunable Antennas," *Progress In Electromagnetics Research C*, Vol. 26, 29-42, 2012.

[24] Chen et al, "Dual-band high-gain Fabry–Perot cavity antenna with a shared-aperture FSS layer," *IET Microwaves, Antennas & Propagation*, vol. 12, no. 13, pp. 2007-2011, 2018.

[25] S. Sun, K. Y. Yang, C. M. Wang, et al, "High-efficiency broadband anomalous reflection by gradient meta-surfaces," *Nano Lett*., vol. 12, no. 12, pp. 6223 6229, 2012.

[26] N. Liu, L. Langguth, T. Weiss, J. Käste, M. Fleischhauer, T. Pfau, and H. Giessen, "Plasmonic analogue of electromagnetically induced transparency at the Drude damping limit," *Nature Materials*, vol. 8, no. 9, pp. 758-762, Jul. 2009.

[27] W. Cao, R. Singh, I. A. I. Al-Naib, M. He, A. J. Taylor, and W. Zhang, "Low-loss ultra-high-Q dark mode plasmonic Fano metamaterials," *Opt. Lett.*, vol. 37, no. 16, pp. 3366-3368, Aug. 2012.

[28] Y. Fan, Z. Wei, H. Li, H. Chen, and C. M. Soukoulis, "Low-loss and high-Q planar metamaterial with toroidal moment," *Phys. Rev. B*, vol. 87, no. 11, pp. 115417, Mar. 2013.

[29] T. Xiang, T. Lei, S. Hu, J. Chen, X. Huang, and H. Yang, "Resonance transparency with low-loss in toroidal planar metamaterial," *J. Appl. Phys.*, vol. 123, no. 9, pp. 095104, Mar. 2018.

ULSAN NATIONAL INSTITUTE OF SCIENCE AND TECHNOLOGY

[30] S. Yang, C. Tang, Z. Liu, B. Wang, C. Wang, J. Li, L. Wang, and C. Gu, “Simultaneous excitation of extremely high-Q-factor trapped and octupolar modes in terahertz metamaterials,” *Optics Express*, vol. 25, no. 14, pp. 15938-15946, Jul. 2017.

[31] J. Liang, K. Tong, and Q. Pei, “A Water-Based Silver-Nanowire Screen-Print Ink for the Fabrication of Stretchable Conductors and Wearable Thin-Film Transistors,” *Advanced Materials*, vol. 28, no. 28, pp. 5986-5996, May 2016.

[32] T. Kaelberer, V. A. Fedotov, N. Papasimakis, D. P. Tsai, and N. I. Zheludev, “Toroidal Dipolar Response in a Metamaterial”, *Science*, vol. 330, no. 6010, pp. 1510-1512, Dec. 2010.

[33] X. Chen and W. Fan, “Study of the interaction between graphene and planar terahertz metamaterial with toroidal dipolar resonance,” *Opt. Lett.*, vol. 42, pp. 2034-2037, May 2017

[34] Autodesk Fusion 360 (2.0.7421). Autodesk. Accessed: Jan. 6, 2020. Available: https://www.autodesk.com/products/fusion-360.

© 2020 IEEE. Reprinted, with permission, from: T. H. Nguyen, H. Y. Jeong, Y. C. Jun and G. Byun, "Geometry-Independent Excitation of Dark Modes Using Dipole Moment Transitions," in *IEEE Transactions on Antennas and Propagation*, doi: 10.1109/TAP.2020.2983770.

ULSAN NATIONAL INSTITUTE OF
SCIENCE AND TECHNOLOGY

Acknowledgment

This work was supported by the New Faculty General Research Fund (1.180044.01) of UNIST (Ulsan National Institute of Science & Technology) and Basic Science Research Program through the National Research Foundation of Korea (NRF) funded by the Ministry of Science, ICT & Future Planning (NRF-2018R1C1B5041 286).

I wish to express my deepest gratitude to my advisor, Professor Gangil Byun, who guided, supported, and encouraged me, who gave me positive energy to go through the hard times of research. Without his conscientious help, this work would not have been accomplished.

I also would like to acknowledge the invaluable assistance that all of ATL's members provided during my study.

Final but not least, I am indebted to my family, who have been always respecting and supporting all of my decisions. Their encouragements were irreplaceable for the success of this work.

This is a slightly modified version of "Geometry-Independent Excitation of Dark Modes Using Dipole Moment Transitions" published in IEEE Transactions on Antennas and Propagation.

ULSAN NATIONAL INSTITUTE OF SCIENCE AND TECHNOLOGY

Appendix

Design procedure

The following is an example design procedure of the original geometry (State 1): we first design a single square loop, composed of two strips as indicated in Appendix Fig. 1 (a), and we will denote this structure as a single-sided cell (SSC) for ease of explanations. Each metallic strip of the SSC is designed to have electrical length of, approximately, half wavelength at resonant frequency to support the strong interaction with the incident waves. This SSC brings a magnetic dipole moment in +z-direction due to the circulation on the strips, and the geometry expands to a double-sided cell (DSC) by mirroring the structure about the vertical plane as shown in Appendix Fig. 1 (b). When s_u is equal to zero, the left side of the DSC produces another magnetic dipole moment in the opposite direction, and its magnitude is almost identical due to symmetry. As a result, a toroidal dipole moment is excited in +y-direction because of the coupling between the two closely spaced magnetic dipoles, which operates as a two-dimensional toroid. For a non-zero s_u, the geometry becomes asymmetric in both planes and produces tri-band resonances of electric quadrupole, toroidal dipole, and Fano resonances. In the proposed design, the electric quadrupole moment is excited by destructive interference between two toroidal dipoles oscillating out-of-phase. More specifically, the upper strips operate as a two-dimensional toroid that accompanies to a toroidal dipole moment in +y-direction, and the lower strips generates another toroidal dipole in −y-direction with a similar magnitude, which destructively interfere with each other

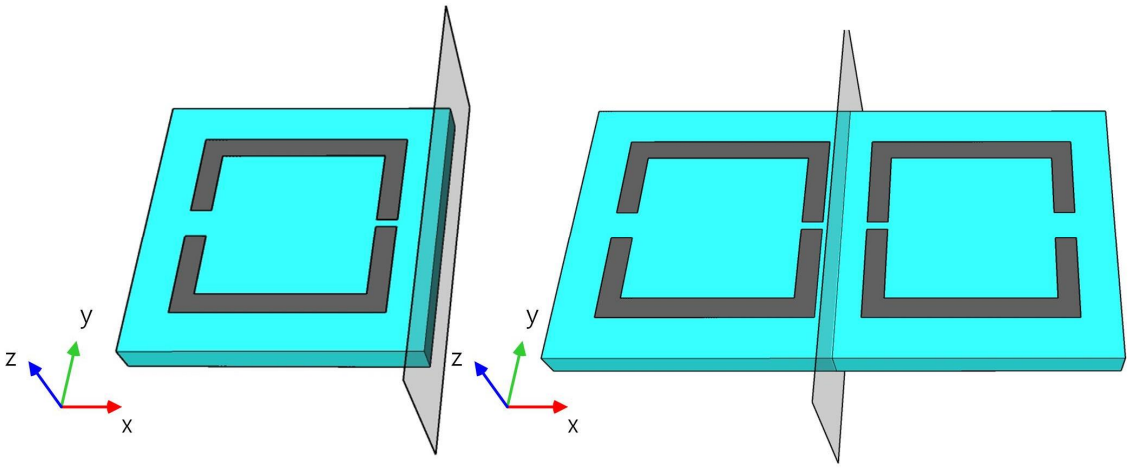

Appendix Fig. 1: Design procedure: (a) Single-sided cell (SCC), (b) Double sided cell (DSC).

ULSAN NATIONAL INSTITUTE OF
SCIENCE AND TECHNOLOGY